Microchimica Acta (2020) 187:262
https://doi.org/10.1007/s00604-020-4223-x

ORIGINAL PAPER

A layered nanocomposite of laccase, chitosan, and Fe_3O_4 nanoparticles-reduced graphene oxide for the nanomolar electrochemical detection of bisphenol A

Paula M. V. Fernandes[1] · José M. Campiña[1] · A. Fernando Silva[1]

Received: 14 October 2019 / Accepted: 7 March 2020

Abstract

A hybrid conjugate of reduced graphene oxide/ferrous-ferric oxide nanoparticles (rGO-Fe_3O_4 NPs) is characterized and assembled with chitosan and laccase to form a layered functional superstructure. After its characterization by field-effect scanning electron microscopy, energy-dispersive X-ray analysis, X-ray photoelectron spectroscopy, attenuated total reflectance Fourier transform infrared, cyclic voltammetry (CV), and electrochemical impedance spectroscopy (EIS), the nanocomposite has been deposited on glassy carbon for the enzyme-mediated electrochemical determination of the endocrine disruptor bisphenol A (BPA). Proof-of-concept assays conducted by using CV, EIS, and square wave voltammetry reveal that the enzymatic biosensor provides linear response in a wide range of BPA concentrations (6–228 ppb), very high sensitivities, and excellent durability (over 1-month storage). Using amperometric detection, remarkable sensitivities (2080 μA μM^{-1} cm^{-2}) and detection limits (18 nM) are attained. Applications to real samples of bottled water proved feasible with recoveries in the range 107–124%.

Keywords Graphene nanomaterials · Graphene-nanoparticle conjugates · Magnetite nanoparticles · Enzymatic biosensors · FESEM · XPS · ATR-FTIR · Cyclic voltammetry · Square wave voltammetry · Electrochemical impedance spectroscopy · Chronoamperometry

Introduction

The 2,2-bis(4-hydroxyphenyl)propane (aka bisphenol A or BPA) is one of the most ubiquitous endocrine disruptors (EDs). Its ability to bind intracellular estrogen receptors (ERα, ERβ, and ERRγ) even at minimal doses [1, 2] may induce reproductive dysfunctions, increase risks of cancer, etc. [3, 4]. BPA has been found in consumer items (plastic food trays and baby bottles, beverage cans, etc.) by solid-phase micro-extraction, gas/liquid chromatography-mass spectrometry, fluorescence spectroscopy, etc. [5–7]. However, other approaches based on miniaturized electroanalytical platforms seem more suitable for any environmental tracing of pollutants due to their low cost, reduced size, portability, high sensitivity, and rapid response. Reduced graphene oxides (rGO) exhibit well-balanced surface-to-volume ratio, electrical conductivity, and electrocatalytic activity to serve as conductivity/charge transfer enhancer in nanostructured coatings to improve the response of classic electrodes [8].

Strong synergies are obtained by conjugation with metallic/semiconducting nanoparticles (NPs) endowed with their own optoelectronic, catalytic, or magnetic properties [9]. Thereby, the incorporation of rGO-NP hybrids (NP: Au, Ni, TiO_2, etc.) to electrochemical sensors has improved their sensitivity to the levels of laboratory methods based on much more expensive equipment and highly skilled personnel [10–13]. Non-enzymatic electrochemical sensors have exhibited high sensitivity (*S*) and low limits of detection (LODs) in the determination of BPA. For instance, Yu et al. reported values of 0.374 μA μM^{-1} cm^{-2} and 8 nM, respectively, using a chitosan-Fe_3O_4 NP composite [14]. The incorporation of rGO or multi-walled carbon nanotubes (MWCNTs) has led to further improvements. Han et al. reported a LOD of 1.7 nM for a

Electronic supplementary material The online version of this article (https://doi.org/10.1007/s00604-020-4223-x) contains supplementary material, which is available to authorized users.

✉ José M. Campiña
jpina@fc.up.pt

[1] Department of Chemistry and Biochemistry, Faculty of Sciences, Centre for Research in Chemistry of The University of Porto (CIQUP), Rua do Campo Alegre 687, 4169-007 Porto, Portugal

Published online: 08 April 2020

MWCNT-acrylamide composite [15] and Su et al. demonstrated an ultrahigh $S = 56.15\ \mu A\ \mu M^{-1}\ cm^{-2}$ using a film of the hybrid rGO-AuPd NP conjugate [10].

Lower LOD in the pM scale was attained with a multilayered superstructure of N-doped rGO and melamine [16]. Using high-capture biological probes (e.g., aptamers [17–19] or peptides [20]) as receptors has also led to lower LODs in the pM–aM range. However, high costs and slow response (hours–days) limit their application in commercial portable/disposable solutions. Intrinsically more sensitive electrical/opto-analytical platforms like field-effect transistors (FETs) [21] or fluorescence resonance energy transfer systems (FRET) [22] have also exhibited LODs in the fM–aM scale, but these are, by far, less cost-effective. A very common issue in non-biological sensors remains its limited molecular selectivity in complex samples. In this sense, the high efficiency and selectivity of enzymes turn enzymatic biosensors much more desirable. While redox enzymes acting on phenols such as tyrosinases (TYRs) or horseradish peroxidase (HRP) present low structural stability and self-inhibition issues, or, in the case of HRP, require hydrogen peroxide to perform, laccases are more stable and, like TYRs, oxidize diphenols in the presence of oxygen (no additional co-factors required) [23–27].

Despite these advantages, only a few BPA laccase-based electrochemical sensors (LES) have been reported in the literature [28–30]. This work introduces a LES for aqueous BPA based on rGO-Fe_3O_4 NPs (nanomagnetites are inexpensive and provide large surface areas and improved biocompatibility [31–34]), chitosan, and laccase. The layered nanocomposite was assembled onto glassy carbon and tested in cyclic voltammetry (CV), square wave voltammetry (SWV), electrochemical impedance spectroscopy (EIS), and chronoamperometric (CA) assays mediated by $[Fe(CN)_6]^{3-/4-}$ [11, 35]. The good biocompatibility of chitosans is expected to enhance the stability of laccase, and the synergistic effects at rGO-Fe_3O_4 NPs should improve the electron transfer (ET) processes/conductivity across the films. The biosensor achieved excellent electroanalytical performance and stability. Good reproducibility and selectivity were attained too. Additional testing in bottled water stocks supplied satisfactory results.

Experimental

Materials and methods

Disodium hydrogen phosphate dihydrate (≥ 98%; $Na_2HPO_4{\cdot}2H_2O$), potassium dihydrogen phosphate (≥ 98%; KH_2PO_4), sodium chloride (≥ 99%; NaCl), bisphenol A (≥ 99%), catechol (≥ 99%), 4-nitrophenol (≥ 99%), glacial acetic acid (≥ 99.85%), and laccase from *Trametes versicolor* (> 0.5 U mg^{-1}) were acquired from Sigma-Aldrich (St. Louis, MO, USA). Ethanol (96% vol.; Aga), potassium hexacyanoferrate(II) trihydrate (p.a.; Fluka; $K_4[Fe(CN)_6]{\cdot}3H_2O$), potassium hexacyanoferrate(III) (p.a.; Fluka; $K_3[Fe(CN)_6]$), N_2 (N45, Air Liquide), sodium acetate trihydrate (suprapur; Merck), D(+)-glucose (99%; Merck), 1-naphthol (99%; Riedel-de Haën), benzene (p.a.; Merck), and chitosan ChitoClear TM2455 (deacetylation degree, DD = 95%; molecular weight 150–200 kDa; Primex) were used as received. Solutions and buffers were prepared in ultrapure water (Milli-RO3 Plus; resistivity 18.2 MΩ cm) and stored at 4 °C.

X-ray photoelectron spectroscopy (XPS), field-effect scanning electron microscopy (FESEM), and energy-dispersive X-ray analysis (EDX) were performed at CEMUP (Centro de Materiais da Universidade do Porto). A Kratos Axis Ultra HSA equipped with an achromatic Al (K_α) X-ray source (15 kV, 90 W) and a 500-mm Rowland circle monochromator was used for XPS measurements. The spectra were analyzed with the CasaXPS software (v.2.3.18PR1.0) using Shirley-type backgrounds. An FEI Quanta 400FEG Genesis X4M Microscope was used for FESEM and EDX. Attenuated total reflectance Fourier transform infrared (ATR-FTIR) spectra were taken using a Bruker Tensor 27 spectrometer. Electrochemical experiments were conducted with a Voltalab PGZ301 potentiostat (Radiometer Analytical). Pt and Ag wires were used as counter and pseudo-reference electrodes. The presence of the $[Fe(CN)_6]^{4-/3}$ probes allowed for an internal calibration of the pseudo-reference electrode (the half-wave potentials derived from the CVs, $E_{1/2}$, matched the standard potential tabulated for the pair, E^O versus Ag/AgCl/NaCl sat). The electrolytes were de-aerated with N_2 before measurements.

Synthesis and characterization of rGO-Fe_3O_4 NPs

The hybrid conjugate was synthesized following a method reported elsewhere [36, 37]. Briefly, graphite flakes were dispersed in H_2SO_4 and heated at 98 °C (30 min) in the presence of $NaNO_3$ and $KMnO_4$ (find more details in Sections S1 & S2†). H_2O_2 was added and the mixture was centrifuged at 3000 rpm in a Beckman system (relative centrifugational force, RCF = 1006×*g*). The graphene oxide (GO) solid was filtered, washed, and re-dispersed in ethanol at 0.5 mg mL^{-1}. 1,2-Hexadecanediol, oleic acid, cis-1-amino-9-octadecene, and iron (III) acetylacetonate (1.7:1:1:0.3 molar ratio) were added into 22 mL of phenyl ether and heated at 200 (30 min) and 265 °C (45 min) in N_2 atmosphere. The resulting dark brown mixture was cooled down and, after the addition of ethanol, centrifuged at 15000 rpm (RCF = 25,155×*g*).

The rGO-Fe_3O_4 NP hybrid was synthesized in one pot by alkaline reduction. For these purposes, the powder was re-dispersed in the 0.5-mg mL^{-1} GO suspension. Citric and ascorbic acids were added, and the mixture was stirred at

55 °C (12 h). NaOH 1 M was added and the mixture was stirred again at 95 °C (6 h). After centrifugation at 10000 rpm (RCF = 1118×*g*), the solid was filtered, washed, and vacuum dried (24 h). The composition, morphology, and crystallinity of the synthesized species were investigated with XPS, ATR-FTIR, FESEM, EDX, and electrochemical techniques. In most of these experiments, the conjugate was deposited onto Si wafers and/or onto a glassy carbon electrode (GCE, Metrohm, 4-mm diameter) from a 0.5-mg mL^{-1} ethanolic dispersion. ATR-FTIR spectra were taken from the pure powder.

Nanocomposite assembly

The GCE was polished with alumina slurry (0.3 μm, Buehler Micropolish II) and thoroughly sonicated in water, ethanol, and acetone. The bionanocomposite film was mounted on it following the sequential drop-casting procedure depicted in Scheme 1. Briefly, 10 μL of 10 mg mL^{-1} dispersion of rGO-Fe_3O_4 NPs in ethanol was spread and dried in the air. In the second step, 10 μL of 5 mg mL^{-1} dispersion of chitosan DD = 95% (hereinafter Chit95) in 0.1 M acetate buffer (AB) at pH 5 was subsequently casted. Once dried, 10 μL of a 10 mg mL^{-1} solution of laccase from *Trametes versicolor* (TvL) in 0.1 M AB (pH 4.5) was dropped. The layer-by-layer construction of the film was monitored by electrochemical measurements in 2 mM $[Fe(CN)_6]^{3-/4-}$ solution in 0.05 M phosphate buffered saline (150 mM NaCl; PBS) at pH 7.4. CVs were acquired at 0.05 V s^{-1} in the range − 0.3/+ 0.6 V. Impedance spectra were recorded at + 0.15 V using a sine wave of 10-mV amplitude and frequency in the range 10^4–10^{-1} Hz. The EIS data were fitted to a R_1QR_2W Randles-type equivalent circuit (see Section S4†). The structure and morphology of the films were inspected by FESEM. Chit95, TvL, rGO-Fe_3O_4 NPs, and rGO-Fe_3O_4NP/Chit95 films were also assembled on GCE for comparison purposes.

Electrochemical determination of BPA

Three independent replicas of the GCE/rGO-Fe_3O_4NP/Chit95/TvL electrode were fabricated and interrogated in 0.1 M AB (pH 4.5) + 2 mM $[Fe(CN)_6]^{3-/4-}$ + BPA (concentration range, BPA 0.05–25 μM) by CV (potential window − 0.3/+ 0.6 V; scan rate 0.050 V s^{-1}), EIS (measurements taken at the cathodic peak potential, i.e., $E_{PC} \approx 0.050$ V in all cases; frequency range 10^4–10^{-1} Hz; amplitude 10 mV), and SWV (cathodic scans of 1-s duration from + 0.6 to − 0.3 V; scan rate 0.015 V s^{-1}; amplitude 15 mV). The relevant parameters derived from these measurements (current density, charge transfer resistance, or differential current density), given as *mean value* ± MSE (standard error of the mean), were plotted against BPA. The calibration curves were obtained by linear regression of the average experimental data and the slopes were taken as the average sensitivity (*S*). The LODs were estimated from the linear regression data:

$$\mathrm{LOD} = 3.3 \times SE_y / S_{\mathrm{sub}-\mu\mathrm{M}} \quad (1)$$

where SE_y and $S_{\text{sub-}\mu\text{M}}$ are the standard error of the *y*-intercept and the slope in the sub-μM domain, respectively (more details in Section S7†). Chroamperometric (CA) curves were also recorded at + 0.15 V in the same electrolyte but in the lower BPA range of 0.025–25 nM. In this case, the LOD was estimated as the BPA providing a cutoff signal of 3 times the signal-to-noise ratio (S/N). Noise and peak signals were measured as indicated in Fig. S10A†, and the LOD was calculated as shown in Fig. S10B†. For practical applications, commercial sport polycarbonate bottles (1 L) were filled with ultrapure water and warmed at 100 °C in a lab oven for 2 weeks. Afterwards, aliquots were buffered at pH 4.5 in the presence of 0.1 M AB + 2 mM $[Fe(CN)_6]^{3-/4-}$ and subsequently spiked to BPA levels of 15 and 30 μM. When not in use, the biosensor was stored at 4 °C in 0.05 M PBS (pH 7.4).

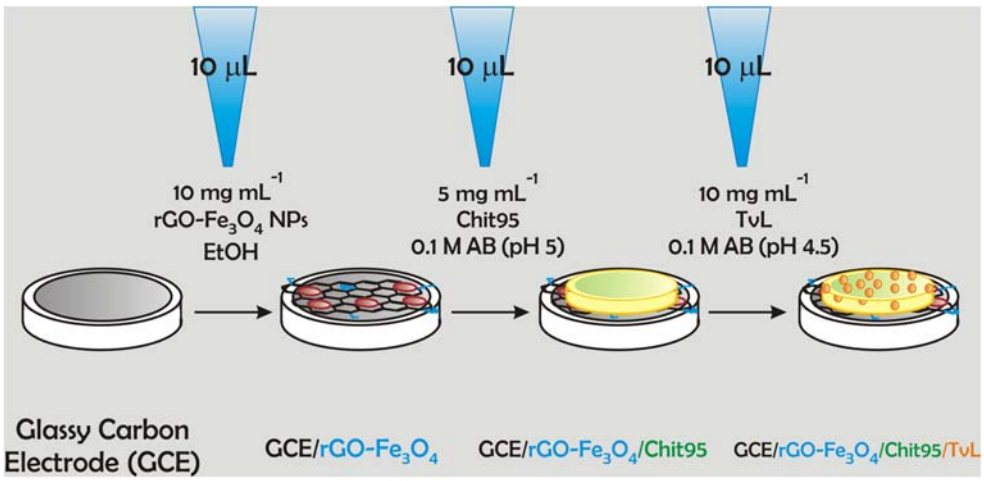

Scheme 1 Sequential drop-casting procedure followed for the modification of the GCE with rGO-Fe_3O_4NP/Chit95/TvL nanocomposite films

Results and discussion

Physicochemical characterization of rGO-Fe_3O_4 NPs

The ATR-FTIR spectrum recorded for the commercial rGO shows no peaks in the range 600–1800 cm^{-1} (black solid line in Fig. 1a). In contrast, the synthesized hybrid (red) exhibits a series of peaks which are assigned as follows: (a) signals at 588 and 667 cm^{-1} due to the stretching of Fe-O bonds in Fe_3O_4 NPs [38]; (b) peaks at 1085, 1115, and 1153 cm^{-1} ascribed to the stretch of hydroxyl-substituted C atoms (C-O and C-C vibrations) in rGO and/or the NP organic shell [39–41]; (c) bands at 1395 and 1635 cm^{-1}, also found for GO [11], attributed to stretching in restored sp^2 C atoms (=C-H and C=C, respectively [42]) or to in-plane C-H bending in $–CH_3$ groups at the NP shell (the 1338-cm^{-1} peak would account for analogous bending at skeletal $–CH_2–$ groups [38]).

Other characteristic peaks of GO, e.g., those at 1220 (asymmetric C-O-C stretching in epoxides) and 1730 cm^{-1} (asymmetric stretching of C=O) [40, 43, 44], are not found in the acquired spectrum, which confirms a significant reduction to rGO. This interpretation is reinforced by the elemental analysis. The wide XPS spectrum in Fig. 1b displays bands at 285 (C 1s), 530 (O 1s), and 710 eV (Fe 2p). By de-convoluting the C 1s core-level spectrum (Fig. S2†), a major peak at 284.5 eV (red curve) is distinguished with shoulders at 285.7 and 288.3 eV. Agreeing with that shown for rGO-Ni NP conjugates [11], these signals have been ascribed to bonds involving restored sp^2 C atoms in the rGO (C=C, C-O, and C=O, respectively). The splitting of the Fe 2p photoemission in its Fe $2p_{1/2}$ and $2p_{3/2}$ components (peaks at 710.4 and 724.3 eV, see Fig. S4†) indicates the co-existence of Fe(II) and Fe(III) redox states as previously reported for Fe_3O_4 [42].

The FESEM top view taken for a GCE modified with rGO-Fe_3O_4 NPs (Fig. S5†) shows a homogeneous distribution of bright particles with coverage under the monolayer. The greatest fraction of these particles displays sizes below 1 μm. By zooming on one of the smallest ones (Fig. 1c), 2D sheets of graphene loaded with spherical NPs were observed. The NP size (15–60 nm) agrees well with that found in previous studies for Fe_3O_4 NPs [45, 46]. In addition, the morphology of the hybrid was nearly identical to that imaged for rGO-Ni NPs [31]. The EDX spectrum confirms the presence of C, O, and Fe (Fig. S6†). In fact, the two pairs of peaks registered for the latter at high (6.5 and 7.1 keV) and low energies (0.6 and 0.75 keV) suggest, again, the occurrence of Fe(III) and Fe(II) (as expected for Fe_3O_4 NPs [45, 46]).

Assembly of the rGO-Fe_3O_4NP/Chit95/TvL nanocomposite

The electrochemical response of the redox probes at the different stages of modification of the GCE is shown in Fig. 2.

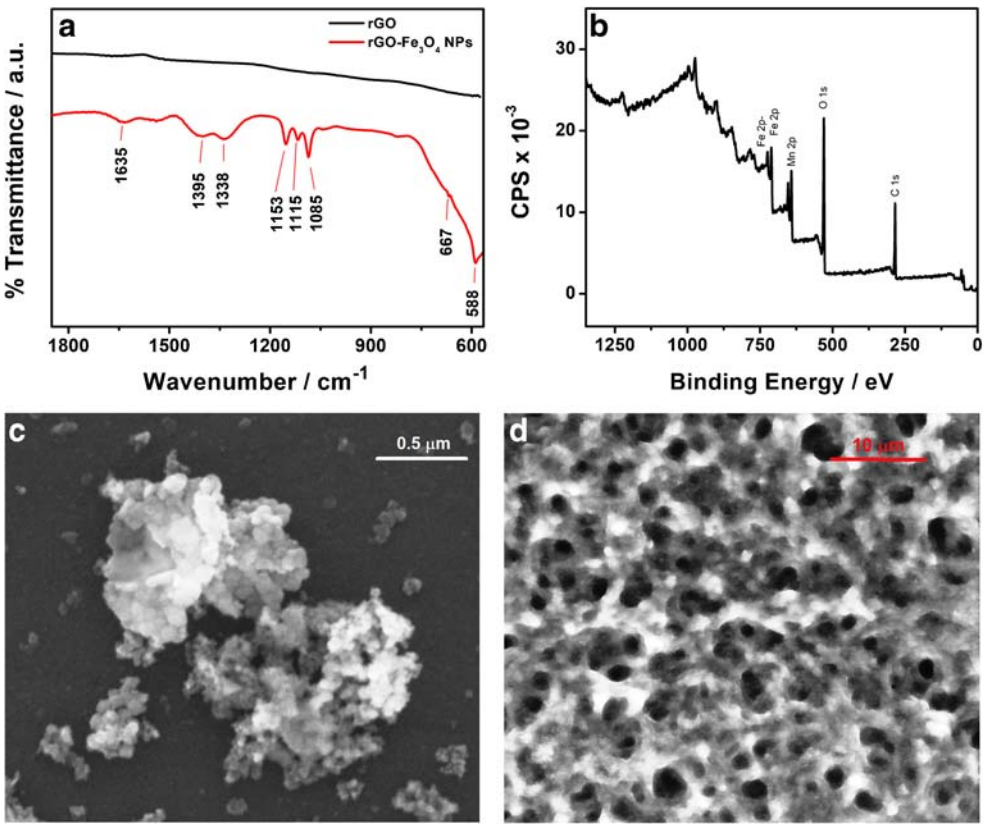

Fig. 1 ATR-FTIR (**a**) and wide XPS (**b**) spectra obtained for the rGO-Fe_3O_4 NP conjugate. The black curve in **a** corresponds to a commercial rGO powder sample included for comparison. FESEM top views of the GCE/rGO-Fe_3O_4 NP (**c**) and the GCE/rGO-Fe_3O_4NP/Chit95/TvL (**d**) modified electrodes (magnification factors × 100,000 and × 5000, respectively)

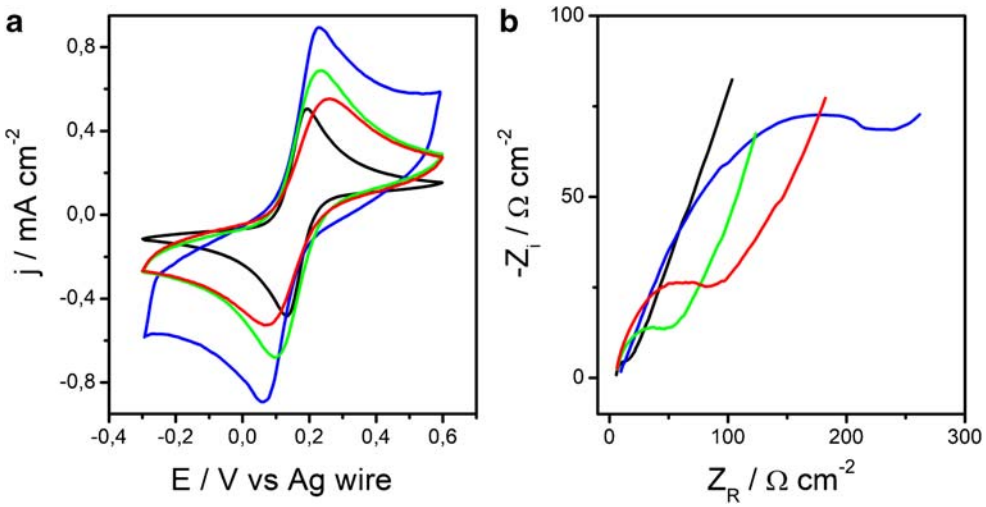

Fig. 2 **a** CVs recorded at 0.05 V s^{-1} in PBS 0.05 M (pH 7.4) + 2 mM $Fe(CN)_6^{3-/4-}$ for bare GCE (black solid line), GCE/rGO-Fe_3O_4 NPs (blue), GCE/rGO-Fe_3O_4NP/Chit95 (green), and GCE/rGO-Fe_3O_4NP/Chit95/TvL (red). **b** Nyquist plots acquired in same conditions at + 0.15 V (oscillation amplitude 10 mV)

The CV of bare GCE (black curve in Fig. 2a) exhibits a very low peak-to-peak potential difference ($\Delta E_P = 60.5$ mV), and its Nyquist (Fig. 2b) features the smallest semicircle of the series. These findings, together with the low apparent charge transfer resistance, R_2, derived from the fittings (210 Ω), confirm the high reversibility of the $[Fe(CN)_6]^{3-/4-}$ pair on GCE. Both the faradaic and non-faradaic components of the current density (j) are clearly boosted in the CV of GCE/rGO-Fe_3O_4 NPs (blue curves). As one may expect from the high surface-to-volume ratio of rGO and the large surface area of Fe_3O_4 NPs, this behavior reflects a huge increase in the electroactive area. The deposition of Chit95 (green) drove a slight decrease of the CV peaks due to the partial passivation of the active sites created in the previous step. Nevertheless, the ET processes were still slightly favored as indicated by the drop of ΔE_P and R_2 from 171 mV and 11.7 kΩ to 139 mV and 0.89 kΩ (a more in-depth discussion is included in Section S5.2†).

The ET processes became slightly more hindered at the fully assembled GCE/rGO-Fe_3O_4NP/Chit95/TvL electrode. This is supported by the small decrease of the peak currents in Fig. 2a (red curve) but also by the increase of ΔE_P and R_2 to values of 188 mV and 1.61 kΩ. Such a behavior is in striking contrast with the dramatic blockage of the electroactivity registered for GCEs coated with either TvL (Fig. S9†) or glucose oxidase enzymes [11]. The radical improvement in the structural stability of the TvL macromolecules accommodated within the biopolymeric network (compared with its rapid unfolding onto bare GCE) is mostly explained by: (1) the great biocompatibility of chitosans with high DD (the high content in hydroxyl and amino groups favors their interaction with the hydrophilic outer regions of proteins, thus stabilizing their native states [47]) and (2) the space constraints imposed by the polymeric scaffold and their crucial role in arresting the physical unfolding of the enzyme. The assembled films were also inspected by FESEM imaging. In this regard, Fig. 1d shows the surface of a GCE entirely covered by a thick and uniform polymer-like film of spongy morphology (pore size in the range 0.5–4.5 μm).

Electrochemical response to BPA

Three replicates of the GCE/rGO-Fe_3O_4NP/Chit95/TvL electrode were prepared and interrogated versus aqueous BPA in proof-of-concept electrochemical tests. Figure 3a–c present the recorded CVs, Nyquist plots, and reverse SWVs. Laccases are known to catalyze elemental one-electron (1e-) oxidation reactions in p-diphenols and analogs:

$$\text{Lacc} + \text{OH–Ph–OH} \rightarrow \text{Lacc}\cdot + \text{HO–Ph–O}\cdot + \text{H}^+ \quad (2)$$

In biological media, molecular O_2 is the typical electron acceptor that regenerates the enzyme. Nevertheless, in the de-aerated electrolytes used in this work, the redox probes play such role. As a consequence, a feedback loop is established through which a good part of the Fe(III) generated at the anodic peak of Fig. 3a is reduced back to Fe(II):

$$\text{TvL}\cdot + \left[\text{Fe(CN)}_6\right]^{3-} \rightarrow \text{TvL} + \left[\text{Fe(CN)}_6\right]^{4-} \quad (3)$$

According to this mechanism, any significant increase in BPA should lead to an increase of the oxidative current and a decline of the reductive one. This is in full agreement with the results presented in Fig. 3a: i.e., while the anodic peak current density (j_{PA}) increases slightly, its cathodic counterpart (j_{PC}) experiences a rather steep drop. In this sense, the differential peak current densities (dj_P) derived from the cathodic SWV scans in Fig. 3c follow an analogous decay. All replicas of the electrode reproduced this behavior (see quantitative data in Section S6†), demonstrating a good reproducibility in

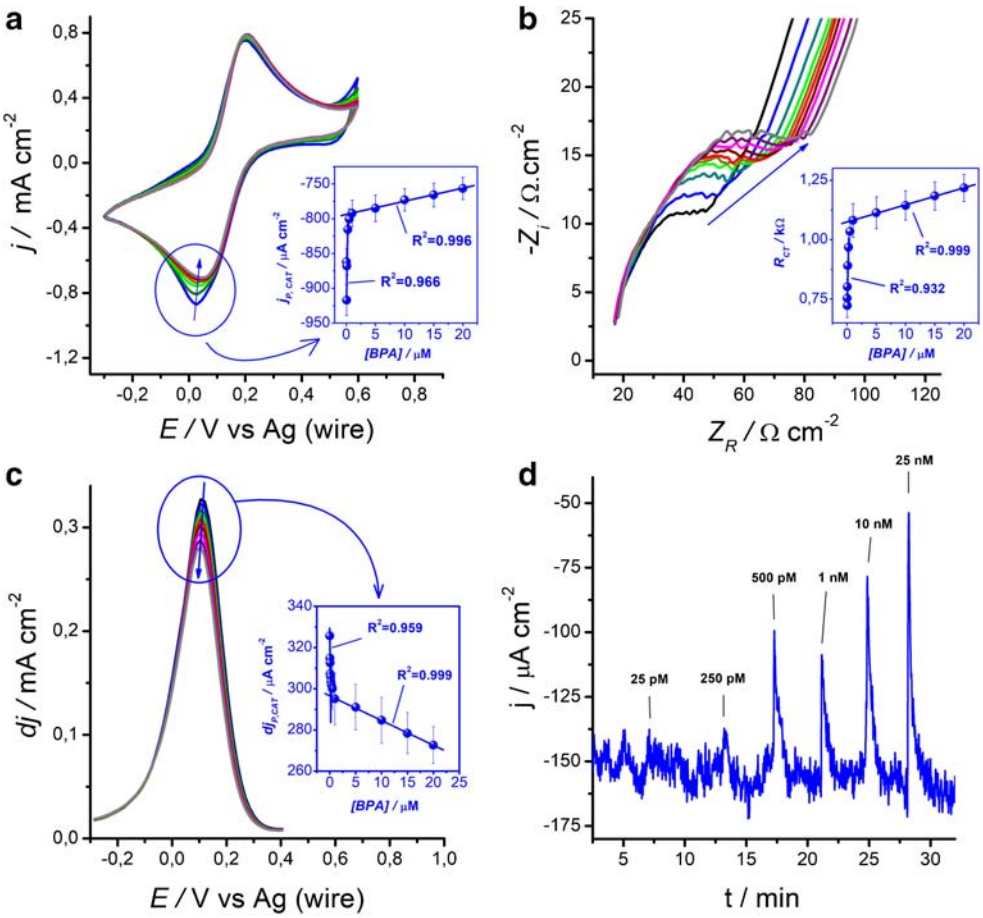

Fig. 3 CV (**a**), EIS (**b**), and SWV (**c**) interrogation of the GCE/rGO-Fe_3O_4NP/Chit95/TvL biosensor in AB 0.1 M (pH 4.5) + 2 mM $Fe(CN)_6^{3-/4-}$ + BPA in the following concentrations: 0.025 (black solid curves), 0.050 (blue), 0.100 (olive), 0.250 (green), 0.500 (orange), 1 (red), 5 (wine), 10 (magenta), 15 (purple), and 20 μM (gray). The means j_{PC}, R_2, and dj_{PC}, with corresponding error bars (given as the standard error of the mean; MSE) and linear regression curves, are displayed in the blue insets. **d** Chronoamperometric measurements in the same medium at + 0.15 V (BPA = 0.025–25 nM). Scan rate 0.050 (**a**) and 0.015 mV s^{-1} (**c**). Amplitude 10 (**b**) and 15 mV (**c**)

the preparation of the sensor. By plotting the mean j_{PC} and mean dj_{PC} versus BPA (blue insets in Fig. 3a, c), two linear domains can be identified.

The first one operates in the submicromolar (sub-μM) concentration range (0.025–1 μM) and may be exploited in the detection of traces of BPA in water samples (clinical, food, or environmental, e.g., effluent discharges from wastewater treatment plants [48]). The second covers a broader range of higher concentrations (1–20 μM) that turns it more appropriate for the analysis of concentrated samples (e.g., effluents from plastic manufacturing plants). The Nyquist plots recorded at the cathodic peak potential (Fig. 3b) show a concomitant growth of the semicircle at mid-high frequency. As detailed in Section S4†, this feature relates to the value of R_2. In good agreement, the mean R_2 versus BPA plot (blue inset) reveals the continuous increase of this parameter along two linear domains identical to those spotted in Fig. 3a, c. Hence, both the voltammetric and impedimetric evidence agree on the progressive hindering of the cathodic process when BPA is increased. As predicted by Eqs. 2 and 3, this behavior confirms that TvL molecules have been immobilized in a fully functional state.

Analytical performance

Regardless of the mode of operation, the sensitivities attained very high values in both concentration domains (Table 1). Nevertheless, those in the sub-μM range are consistently two orders of magnitude higher (with a maximum of 471.3 μA μM^{-1} cm^{-2} in CV mode). LODs of 24, 15, and 11 ppb (103, 65, and 47 nM) have been derived from the

Table 1 Parameters derived by fitting the average data in the sub-μM and μM domains (insets of Fig. 3a–c) to straight lines with formula $Y = A \pm S$ BPA, where Y accounts for either j_{PC}, R_2, or dj_{PC}; A is the y-intercept; S the slope; and R the correlation coefficient

Mode	Domain	BPA (μM)	S (μA μM^{-1} cm^{-2})	A (μA cm^{-2})	R
CV	Sub-μM	0.025–1	471.3	− 930	0.966
CV	μM	1–20	1.890	− 794	0.997
SWV	Sub-μM	0.025–1	228.7	329	0.959
SWV	μM	1–20	1.200	297	0.999
			S (Ω μM^{-1})	A (Ω)	R
EIS	Sub-μM	0.025–1	950.5	746.8	0.936
EIS	μM	1–20	7.180	1075	0.999

CV, EIS, and SWV assays, respectively. These figures fall close, or even below, the BPA levels found, for instance, in waters used for the sterilization of polycarbonate baby bottles (≈ 50 ppb [49]) or in bottled waters stored under different conditions (5–300 ppb [50]). The European Food Safety Authority recommends a tolerable daily intake of 4-μg BPA per kg of body weight (bw) in adults. To reach that dosage merely through water consumption, an individual of 70-kg bw would have to drink 2 L per day of a water containing at least 150 ppb of BPA (a level significantly higher than the LODs discussed above). Therefore, the assays in Fig. 3a–c show good potential for the assessment of the safety of waters stocked at shops, warehouses, logistic centers, etc.

Such a performance constitutes a solid demonstration of the biosensor concept, and, in addition, it can be taken as excellent if the following aspects are considered: (A) the inherent limitations of electroanalytical methods (compared with other more sensitive electrical/optical platforms based on FETs, localized surface plasmon resonance, etc.), (B) the absence of analyte pre-accumulation steps or signal amplification schemes, (C) the limited enzyme loading capacity of a single rGO-Fe_3O_4NP/Chit95-TvL bilayer, (D) the heterogeneous distribution of resistivity across the films (good electrical properties are mostly localized at the inner rGO-Fe_3O_4 NP layer), and (E) the limited stability of proteins at solid surfaces and its impact on the outcome of enzymatic biosensors.

The biosensor response was also investigated in a lower concentration range by CA (Fig. 3d). A measurable signal was registered even at BPA levels as low as 5.7 ppt (25 pM). This is relevant since the disruption of cellular processes is triggered at a very low exposure (at levels of ppt) [2]. However, as shown in Section S7.1†, the peaks recorded in this region are statistically indistinguishable from noise and the calculated LOD amounts to 4 ppb (18 nM). These results compare very well with those reported for other electrochemical sensors based on rGO/GO, MWCNTs, polymers, and/or inorganic NPs as signal transducers or supporting materials. In this regard, Table 2 presents the output registered by a number of devices (both enzymatic and non-enzymatic) built off these nanomaterials. In all cases, the reported sensitivities are much lower than those discussed above (the highest one is about 4 and 37 times lower than those derived from SWV and CA, respectively).

Tyrosinase-based enzymatic sensors (TES, entries 5th–7th) attain LDRs very similar to those verified for the GCE/rGO-Fe_3O_4NP/Chit95/TvL biosensor under CV, EIS, or SWV. However, the latter shows extended linearity down to the pM scale (Fig. 3d) and LODs among those reported for the

Table 2 Sensitivity (*S*), limit of detection (LOD), and linear dynamic range (LDR) reported in the literature for the detection of BPA using different enzymatic (E) and non-enzymatic (NE) electrochemical sensors

Technique	Sensor	Type	*S*/ μA μM $^{-1}$ cm^{-2}	LOD/ nM	LDR/μM	Ref.
DPV[a]	GCE/Chit[b]/Fe_3O_4 NPs	NE	0.374	8.000	0.050–30	[14]
DPV	GCE/rGO-Fe_3O_4 NPs	NE	0.256	17.00	0.060–11	[13]
DPV	GCE/rGO-AuPd NPs	NE	56.15	8.000	0.050–10	[10]
CV	GCE/MWCNT[c]/PAAM[d]	NE	30.40	1.700	0.005–20	[15]
DPV	GCE/rGO-AuNP/Chit/Tyr[e]	E	50.89	1.000	0.025–3	[51]
CV	GCE/NGP[f]-Chit-Tyr	E	3.108	33.00	0.100–2	[52]
CA	SPCE/Fe_3O_4NP/Tyr	E	3.199	8.300	0.027–40	[53]
CA	SPCE/CB[g]/Thio[h]/TvL	E	0.071	200.0	0.500–50	[29]
DPV	GCE/3DGN[i]/Cu/Fe_3O_4/TvL	E	5.014	1700	7.200–18	[30]
SWV	GCE/rGO-Fe_3O_4NP/Chit95/TvL	E	228.7	47.00	0.025–20	This work
CA			2080	18.10	2.5×10^{-5}–0.025	
EIS			950.5 Ω μM^{-1}	65.00	0.025–20	

[a] Differential pulse voltammetry

[b] Chitosan

[c] Multi-walled carbon nanotubes

[d] Polyacrylamide

[e] Tyrosinase

[f] Nanographene

[g] Carbon black

[h] Thionine

[i] 3D graphene

TES in the table (1–33 nM). This is important because TvL provides lower self-inhibition, better stability, and the ability to perform in absence of peroxide or oxygen acceptors. To our best knowledge, the best performing LES reported so far (8th entry in Table 2) exhibits a LOD 4–11 times higher than those discussed for the GCE/rGO-Fe_3O_4NP/Chit95/TvL biosensor and a more limited range of linearity (down to only 500 nM).

Reproducibility, durability, and interferences

The error bars in the insets of Fig. 3 represent relative standard errors of 1–3% (CV), 5–8% (EIS), and 2–4% (SWV) (Table S2†). Taking into account the large amount of synthetic and assembly steps comprising the fabrication of the investigated biosensor, these values are very low and indicate a good degree of reproducibility. No signal degradation was observed during the registration of 100 consecutive CVs with a freshly prepared biosensor (Fig. S11A†). The relative standard deviation (RSD) of j_{PA} in these experiments fell below 1.5%, thus showcasing the excellent repeatability and structural integrity of the biosensor under continuous operation. As a proof of its good durability, the j_{PA} only declined by 18% after 1 month of storage at 4 °C in AB 0.1 M (Fig. S11B†).

The impact of potentially interfering species (PIS) such as catechol (CC, an o-diphenol), ascorbic acid (AA), uric acid (UA), glucose (G), 1-naphthol (1-NTHL), 4-nitrophenol (4-NPHL), and benzene (BZ) was investigated in AB 0.1 M + $[Fe(CN)_6]^{3-/4-}$ 2 mM + BPA 10 μM + PIS 0.01–10 μM. By increasing CC, a very small and symmetric decrease was observed in both redox peaks (RSD for j_{PC} 5.5%, Fig. S12A†). A similar effect is found in Figs. S12C, S12E, S12G, S12I, S12K, and S12M† for AA (RSD 0.4%), UA (6.2%), G (9.3%), 1-NTHL (1.8%), 4-NPHL (1.5%), and BZ (2.0%). Very minor changes are also observed in the registered Nyquist plots (Figs. S12B, S12D, S12F, S12H, S12J, S12L, and S12N†). Hence, only glucose seems to pose a really small but significant interference to the biosensor response (relative error well above ± 6%).

Practical application

To explore the potential of the GCE/rGO-Fe_3O_4NP/Chit95/TvL electrode in real-life applications, water samples were bottled and stored at high temperature (see the Experimental section). Aliquots were added to an equal volume of working electrolyte for later analysis by EIS. Three parallel determinations were performed in each case. The average concentration of endogenous BPA determined is 4.94 μM, which falls within the range reported in the literature for aqueous samples incubated with BPA-leaching plastics under similar conditions (4–6 μM) [14, 15, 50]. BPA content was also determined after spiking the samples with 15 and 30 μM obtaining recoveries of 124 and 107%, respectively (RSD = 1.7 and 2.2%). Although further optimization must be required for operation in real samples, the results demonstrate that the biosensor can detect harmful levels of BPA in waters stored in PC bottles.

Conclusions

This paper describes an approach to the immobilization of TvL with a high surface area graphene-nanomagnetite conjugate (signal transducer) and a high-DD chitosan (biocompatible support). The nanocomposite has been tested towards the electrochemical detection of BPA at low potential (< 0.2 V) without pre-accumulation or signal amplification schemes. Under these conditions, the GCE/rGO-Fe_3O_4/Chit95/TvL biosensor exhibits ultrahigh sensitivity (minimum LOD of 4 ppb BPA), wide linearity, and rapid response. To our best knowledge, this is the best performing LES reported so far in the literature. Good reproducibility, durability, and an excellent operational stability have been registered. Among all the investigated PIS, only glucose interferes significantly with the biosensor response (although in a very limited and likely manageable way). At this stage, applications to the analysis of real waters (tap, bottled, stored, effluents from plastic manufacturing industries, etc.) are more feasible than those for more complex samples (e.g., sugar-containing drinks, reconstituted foods, blood serum). In any case, there is plenty of room for improvements in cross-sensitivity and analytical performance (e.g., through the engineering of more homogenous films, rGO-Fe_3O_4NP/Chit95-TvL multilayers). Integration with miniaturized electrochemical technology may bring future solutions for testing the safety of real foods/drinks at a point-of-need.

Acknowledgments We warmly thank Pr. Elby Titus and Dr. Rahul Krishna for their kind donation of a sample of the hybrid conjugate.

Funding information This work was supported by European (FEDER) and National Portuguese funds (COMPETE and POPH programs; Pest-C/EQB/LA0006/2013, PTDC/EME-MFE/103051). PMVF and JMC acknowledge the Fundacão para a Ciência e a Tecnologia de Portugal (FCT) for the concession of a doctoral and a post-doctoral grant (SFRH/BD/111274/2015 and SFRH/BPD/109537/2015).

Compliance with ethical standards

Conflict of interest The authors declare that they have no competing interest.

References

1. Matsushima A, Kakuta Y, Teramoto T, Koshiba T, Liu X, Okada H, Tokunaga T, Kawabata S-I, Kimura M, Shimohigashi Y (2007) Structural evidence for endocrine disruptor bisphenol A binding to human nuclear receptor ERRγ. J Biochem 142:517–524
2. Vom Saal FS, Hughes C (2005) An extensive new literature concerning low-dose effects of bisphenol A shows the need for a new risk assessment. Environ Health Perspect 113:926–933

3. Doherty LF, Bromer JG, Zhou Y, Aldad TS, Taylor HS (2010) In utero exposure to diethylstilbestrol (DES) or bisphenol-A (BPA) increases EZH2 expression in the mammary gland: an epigenetic mechanism linking endocrine disruptors to breast cancer. Horm Canc 1:146–155
4. Tarapore P, Ying J, Ouyang B, Burke B, Bracken B, Ho SM (2014) Exposure to bisphenol A correlates with early-onset prostate cancer and promotes centrosome amplification and anchorage-independent growth in vitro. PLoS One 9(3):e90332
5. Cao XL, Corriveau J (2008) Migration of bisphenol A from polycarbonate baby and water bottles under severe conditions. J Agric Food Chem 56:6378–6381
6. Nerín C, Philo MR, Salafranca J, Castle L (2002) Determination of bisphenol-type contaminants from food packaging materials in aqueous foods by solid-phase microextraction-high-performance liquid chromatography. J Chromatogr A 963:375–980
7. Brenn-Struckhofova Z, Cichna-Markl M (2006) Determination of bisphenol A in wine by sol-gel immunoaffinity chromatography, HPLC, and fluorescence detection. Food Addit Contam 23:1227–1235
8. Yang Y, Asiri AM, Tang Z, Du D, Lin Y (2013) Graphene based materials for biomedical applications. Mater Today 16:365–373
9. Dalfovo MC, Lacconi GI, Moreno M, Yappert MC, Sumanasekera GU, Salvarezza RB, Ibañez FJ (2014) Synergy between graphene and Au nanoparticles (Heterojunction) towards quenching, improving Raman signal, and UV light sensing. ACS Appl Mater Interfaces 6:6384–6391
10. Su B, Shao H, Li N, Chen X, Cai Z, Chen X (2017) A sensitive bisphenol A voltammetric sensor relying on AuPd nanoparticles/graphene composites modified glassy carbon electrode. Talanta 166:126–132
11. Krishna R, Campiña JM, Fernandes PMV, Ventura J, Titus E, Silva AF (2016) Reduced graphene oxide-nickel nanoparticles/biopolymer composite films for the sub-millimolar detection of glucose. Analyst 141:4151–4161
12. Albelda JAV, Uzunoglu A, Santos GNC, Stanciu LA (2017) Graphene-titanium dioxide nanocomposite based hypxanthine sensor for assessment of meat freshness. Biosens Bioelectron 89:518–524
13. Zhang Y, Cheng Y, Zhou Y, Li B, Gu W, Shi X, Xian Y (2013) Electrochemical sensor for bisphenol A based on magnetic nanoparticles decorated reduced graphene oxide. Talanta 107:211–218
14. Yu C, Gou L, Zhou X, Bao N, Gu H (2011) Chitosan-Fe_3O_4 nanocomposite based electrochemical sensors for the determination of bisphenol A. Electrochim Acta 56:9056–9063
15. Han J, Li F, Jiang L, Li K, Dong Y, Li Y (2015) Electrochemical determination of bisphenol A using a polyacrylamide-multiwalled carbon nanotube-modified glassy carbon electrode. Anal Methods 7:8220–8226
16. Qin J, Shen J, Xu X, Yuan Y, He G, Chen H (2018) A glassy carbon electrode modified with nitrogen-doped reduced graphene oxide and melamine for ultra-sensitive voltammetric determination of bisphenol A. Microchim Acta 185:459
17. Mirzajani H, Cheng C, Wu J, Chen J, Eda S, Aghdam EN, Ghavifekr HB (2017) A highly sensitive and specific capacitive aptasensors for rapid and label-free trace analysis of bisphenol A (BPA) in canned foods. Biosens Bioelectron 89:1059–1067
18. Ensafi AA, Amini M, Rezaei B (2018) Molecularly imprinted electrochemical aptasensor for the attomolar detection of bisphenol A. Microchim Acta 185:265
19. Baghayeri M, Ansari R, Nodehi M, Razavipanah I, Veisi H (2018) Voltammetric aptasensor for bisphenol A based on the use of a MWCNT/Fe_3O_4@gold nanocomposite. Microchim Acta 185:320
20. Kim KS, Jang JR, Choe WS, Yoo PJ (2015) Electrochemical detection of bisphenol A with high sensitivity and selectivity using recombinant protein-immobilized graphene electrodes. Biosens Bioelectron 71:214–221
21. Kim SG, Lee JS, Jun J, Shin DH, Jang J (2016) Ultrasensitive bisphenol A field-effect transistor sensor using an aptamer-modified multichannel carbon nanofiber transducer. ACS Appl Mater Interfaces 8(10):6602–6610
22. Zhu Y, Cai Y, Xu L, Zheng L, Wang L, Qi B, Xu C (2015) Building an aptamer/graphene oxide FRET biosensor for one-step detection of bisphenol A. ACS Appl Mater Interfaces 7(14):7492–7496
23. Cajthaml T, Kresinova Z, Svobodova K, Moder M (2009) Biodegradation of endocrine-disrupting compounds and suppression of estrogenic activity by ligninolytic fungi. Chemosphere 75:745–750
24. Abdullah J, Ahmad M, Heng LY, Karuppiah N, Sidek H (2006) Immobilization of tyrosinase in chitosan film for an optical detection of phenol. Sensors Actuators B Chem 114:604–609
25. Abdullah J, Ahmad M, Heng LY, Karuppiah N, Sidek H (2006) Stacked films immobilization of MBTH in nafion/sol-gel silicate and horseradish peroxidase in chitosan for the determination of phenolic compounds. Anal Bioanal Chem 386:1285–1292
26. Rodríguez-Delgado MM, Alemán-Nava GS, Rodríguez-Delgado JM, Dieck-Assad G, Martínez-Chapa SO, Barceló D, Parra R (2015) Laccase-based biosensors for detection of phenolic compounds. TrAC-Trend Anal Chem 74:21–45
27. Freire RS, Duran N, Kubota LT (2002) Development of a laccase-based flow injection electrochemical biosensor for the determination of phenolic compounds and its application for monitoring remediation of Kraft E1 paper mill effluent. Anal Chim Acta 463:229–238
28. Casero E, Petit-Domínguez MD, Vázquez L, Ramírez-Asperilla I, Parra-Alfambra AM, Pariente F, Lorenzo E (2013) Laccase biosensors based on different enzyme immobilization strategies for phenolic compounds determination. Talanta 115:401–408
29. Portaccio M, Di Tuoro D, Arduini F, Moscone D, Cammarota M, Mita DG, Lepore M (2013) Laccase biosensor based on screen-printed electrode modified with thionine-carbon black nanocomposite for bisphenol A detection. Electrochim Acta 109:340–347
30. Lou C, Jing T, Tian J, Zheng Y, Zhang J, Dong M, Wang C, Hou C, Fan J, Guo Z (2019) 3-Dimensional graphene/Cu/Fe_3O_4 composites: immobilized laccase electrodes for detecting bisphenol A. J Mater Res 34(17):2964–2975
31. Dyshlyuk LS, Novoselova MV, Rozalenok TA (2013) Immobilization of chymotrypsin on magnetic Fe_3O_4 nanoparticles. Foods Raw Mater 1:85–88
32. Zhao G, Wang J, Li Y, Chen X, Liu Y (2011) Enzymes immobilized on superparamagnetic Fe_3O_4@clays nanocomposites: preparation, characterization, and new strategy for the regeneration of supports. J Phys Chem C 115:6350–6359
33. Godage OS, Bucharskaya AB, Navolokin NA, Maslyakova GN, German SV, Gorin DA (2017) The magnetite nanoparticles in theranostic applications. J Nanomed Res 5(3):00119
34. Revia RA, Zhang M (2016) Magnetite nanoparticles for cancer diagnosis, treatment, and treatment monitoring: recent advances. Mater Today 19:157–168
35. Borges J, Campiña JM, Silva AF (2013) Chitosan biopolymer-$F(ab')_2$ immunoconjugate films for enhanced antigen recognition. J Mater Chem B 1:500–511
36. Krishna R, Dias C, Ventura J, Titus E (2016) Green and facile decoration of Fe_3O_4 nanoparticles on reduced graphene oxide. Mater Today Proc 3:2807–2813
37. Krishna R, Titus E, Costa LC, Menezes JCJMDS, Correia MRP, Pinto S, Ventura J, Araújo JP, Cavaleiro JAS, Gracio JJA (2012) Facile synthesis of hydrogenated reduced graphene oxide via hydrogen spillover mechanism. J Mater Chem 22:10457–10459
38. Wang J, Meng G, Tao K, Feng M, Zhao X, Li Z, Xu H, Xia D, Lu JR (2012) Immobilization of lipases on alkyl silane modified magnetic nanoparticles: effect of alkyl chain length on enzyme activity. PLoS One 7:e43478

39. Li BJ, Cao HQ (2011) ZnO@graphene composite with enhanced performance for the removal of dye from water. J Mater Chem 21: 3346–3349
40. Lin-Vien D, Colthup NB, Fateley WG, Grasselli JG (1991) The handbook of infrared and Raman characteristic frequencies of organic molecules, 1st edn. Academic Press, London
41. Unnikrishnan B, Palanisamy S, Chen SM (2013) A simple electrochemical approach to fabricate a glucose biosensor based on graphene-glucose oxidase biocomposite. Biosens Bioelectron 39: 70–75
42. Narayanan TN, Liu Z, Lakshmy PR, Gao W, Nagaoka Y, Kumar DS, Lou J, Vajtai R, Ajayan PM (2012) Synthesis of reduced graphene oxide-Fe_3O_4 multifunctional freestanding membranes and their temperature dependent electronic transport properties. Carbon 50:1338–1345
43. Acik M, Lee G, Mattevi C, Chhowalla M, Cho K, Chabal YJ (2010) Unusual infrared-absorption mechanism in thermally reduced graphene oxide. Nat Mater 9:840–845
44. Bharath G, Madhu R, Chen SM, Veermani V, Balamurugan A, Mangalaraj D, Ponpandian N (2015) Enzymatic electrochemical glucose biosensensor by mesoporous 1D hydroxyapatite-on-2D reduced graphene oxide. J Mater Chem B 3:1360–1370
45. Ghasemzadeh MA, Abdollahi-Basir MH, Babaei M (2015) Fe_3O_4@SiO_2-NH_2 core-shell nanocomposite as an efficient and green catalyst for the multicomponent synthesis of highly substituted chromeno[2,3-b] pyridines in aqueous ethanol media. Green Chem Lett Rev 8:40–49
46. Bagbi Y, Sarswat A, Mohan D, Pandey A, Solanki PR (2016) Lead (Pb^{2+}) adsorption by monodispersed magnetite nanoparticles: surface analysis and effects of solution chemistry. J Environ Chem Eng 4:4237–4247
47. Li SS, Tu KH, Lin CC, Chen CW, Chhowalla M (2010) Solution-processable graphene oxide as an efficient hole transport layer in polymer solar cells. ACS Nano 4:3169–3174
48. Corrales J, Kristofco LA, Steele WB, Yates BS, Breed CS, Spencer Williams E, Brooks BW (2015) Global assessment of bisphenol A in the environment: review and analysis of its occurrence and bioaccumulation. Dose Response July–September: 1–29
49. Biedermann-Brem S, Grob K (2009) Release of bisphenol A from polycarbonate baby bottles: water hardness as the most relevant factor. Eur Food Res Technol 228(5):679–684
50. Biles JE, McNeal TP, Begley TH, Hollifield HC (1997) Determination of bisphenol-A in reusable polycarbonate food-contact plastics and migration to food-simulating liquids. J Agric Food Chem 45:3541–3544
51. Pan D, Gu Y, Lan H, Sun Y, Gao H (2015) Functional graphene-gold nano-composite fabricated electrochemical biosensor for direct and rapid detection of bisphenol A. Anal Chim Acta 853:297–302
52. Wu L, Deng D, Jin J, Lu X, Chen J (2012) Nanographene-based tyrosinase biosensor for rapid detection of bisphenol A. Biosens Bioelectron 35:193–199
53. Alkasir RS, Ganesana M, Won YH, Stanciu L, Andreescu S (2010) Enzyme functionalized nanoparticles for electrochemical biosensors: a comparative study with applications for the detection of bisphenol A. Biosens Bioelectron 26:43–49